JACS Au
AN OPEN ACCESS JOURNAL OF THE AMERICAN CHEMICAL SOCIETY

Structural Expansion and Enhanced Photocurrent Conversion of Selenido Stannates with Cu^+ Ions

Zhou Wu, Benjamin Peerless, Panpan Wang, Wolfgang Schuhmann, and Stefanie Dehnen*

Cite This: https://doi.org/10.1021/jacsau.4c00375 Read Online

ACCESS | Metrics & More | Article Recommendations | Supporting Information

ABSTRACT: As a means of tuning the electronic properties of tin-chalcogenide-based compounds, we present a strategy for the compositional and structural expansion of selenido stannate frameworks under mild conditions by introducing Cu^+ ions into binary anionic Sn/Se aggregates in ionothermal reactions. The variable coordination modes of Cu^+—contrasting with tetrahedral $\{SnSe_4\}$ or trigonal bipyramidal $\{SnSe_5\}$ units—and corresponding expansion toward ternary Cu/Sn/Se substructures helped to add another degree of freedom to the nanoarchitectures. As desired, the variation of the structural features was accompanied by concomitant changes of the physical properties. Upon treatment of alkali metal salts of the $[SnSe_4]^{4-}$ anion at slightly elevated temperatures (120 or 150 °C) in ionic liquids, we isolated a series of compounds comprising ternary or quaternary cluster molecules or networks of cluster units, $(C_2C_2Im)_9Li[Cu_{10}Sn_6Se_{22}]$ (**1**), $(C_2C_2Im)_4[Cu_8Sn_6Se_{18}]$ (**2**), $(C_2C_1Im)_3[Cu_5Sn_3Se_{10}]$ (**3**), and $(C_2C_2Im)_5[Cu_8Sn_6Se_{18}F]\cdot(C_2C_2Im)[BF_4]$ (**4**; C_2C_2Im = 1,3-diethyl-imidazolium, C_2C_1Im = 1-ethyl-3-methyl-imidazolium), which were investigated in terms of their optical gaps and photocurrent conversion properties. As illustrated by the synthesis and characterization of an additional salt that does not include Cu^+, $\{(C_2C_2Im)_2[Sn_3Se_7]\}_4\cdot\{(C_2C_2Im)[BF_4]\}_2$ (**5**), the significant role of Cu^+ in this system was shown to be 3-fold: (a) structural expansion, (b) narrowing of the optical gap, and (c) photocurrent enhancement. By this three-in-one effect, the work offers an in-depth understanding of chalcogenido metalate chemistry with atomic precision.

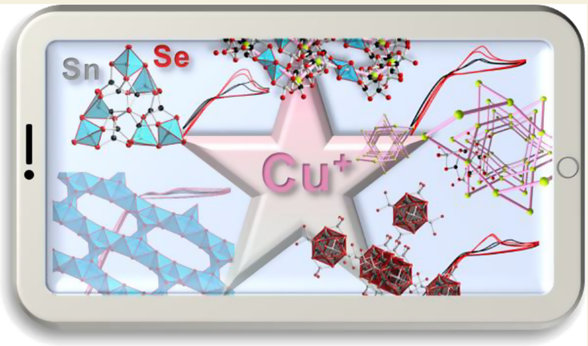

KEYWORDS: *cluster chemistry, compositional expansion, selenido metalates, optoelectronic properties, photocurrent*

1. INTRODUCTION

Given the technical relevance of tin chalcogenides,[1−3] as well as ternary or quaternary expansions of them, metal−tin chalcogenide derivatives are among the most actively studied materials for high-end technologies. Lead tin chalcogenides, $PbSnCh_2$ (Ch=S or Se),[4,5] copper−tin chalcogenides, Cu_2SnCh_3,[6,7] or copper−zinc-tin chalcogenides, $Cu_2ZnSnCh_4$,[8,9] for instance, are highly promising materials for thermoelectric or light-conversion technologies. The subtle impact of the admixture of Cu^+ to tin chalcogenides has been intensely studied, and nanosized versions of corresponding thin films proved to be excellent materials for absorber layers in thin film solar cells.[10−13] However, there are still many open questions regarding the synthetic access of such materials, especially in the context of expansions in the compositions and their crystalline (nano)structures.

One of the strategies for such expansion encompasses the establishment of synthetic approaches to related classes of compounds. Chalcogenido stannates, which are derived from the binary solids, are an example for a very topical field of research in this area in the recent past.[14,15] The goal of these activities is to obtain access to innovative materials with new structural motifs and concomitant physical properties. However, the structural variability in the binary anionic frameworks is limited owing to the strong preference of tetrahedral and trigonal bipyramidal coordination environments of Sn(IV) atoms,[15,16] which was slightly expanded in mixed-valence compounds featuring also trigonal Sn(II) sites.[17] These findings consequently triggered the development of strategies for more effective expansion of compositions and structures.

Multinary, cluster-based crystalline chalcogenido metalates, in particular those exhibiting micropores, have long been regarded as the heavier homologues of zeolites,[18] as they share many commonalities in terms of the synthetic approaches,[19] of their structural subunits,[20] and also of functional applications.[21,22] Anionic zeolite substructures are usually constructed

Received: April 26, 2024
Revised: July 31, 2024
Accepted: August 1, 2024

from aluminates and silicates, in which ammonium or alkali metal countercations serve as structure-directing agents.[23−25] Upon using the heavier congeners of these three main-group elements, typically Ga(III)/In(III), Ge(IV)/Sn(IV), and S(−II)/Se(−II), a wide spectrum of zeolite-type chalcogenido metalate structures could be prepared based on supertetrahedral subunits.[20,26] Besides this, the in situ reduction of Tt(IV) (Tt = Ge or Sn) allowed for the formation of trigonal pyramidal Tt(II) centers, and thus, the isolation of a series of novel ternary and quaternary salts in this system.[27,28]

However, the structural expansion of such compounds has recently experienced a bottleneck period due to the limited types of operable cations and the geometric restrictions of their coordination by chalcogenide ligands. Inclusion of a different kind of atom—like doping if added in small amounts only—is generally accepted as an effective method for manipulating both structures and functional properties of crystalline materials,[29,30] including supertetrahedral chalcogenido metalates.[31,32] Other positive charges, in particular, cause modifications in the composition and structures of the subunits in the crystal lattice. Therefore, the addition of M^{2+} cations like Zn^{2+}, Cd^{2+}, Mn^{2+}, or Fe^{2+}, into the Tt(IV)-Ch(−II) and Tr(III)-Ch(−II) (Tr = Ga or In) systems has proven fruitful.[33−35] However, the coordination geometry of M^{2+} with chalcogenide ligands preferably falls to tetrahedral and continues to be a barrier for further expansion of the family of such compounds to some extent.

As a last aspect, the synthesis conditions play another important role, with high-temperature approaches usually limiting the range of structural variations beyond the most stable versions and solution-based approaches impacting the systems with solvent effects or solubility issues.

To expand the approaches described above, we therefore took advantage of the multiple coordination modes of Cu^+ with chalcogenide ligands,[36−39] and introduced Cu^+ into chalcogenido metalate cluster architectures under mild ionothermal reaction conditions. This way we aimed at partially modifying the coordination patterns to enable variations of the geometric as well as the electronic structures and, therefore, the physical properties. This strategy proved to be promising, even though it would be a challenge to predict the crystal structures of the final products in advance. Scheme 1 illustrates the variety of coordination modes of the ions mentioned above.

Selenido metalates were selected in this study for their higher reactivity than that of sulfido metalates and higher stability than that of tellurido metalates. In regard to the most sustainable materials, the employment of selenido stannates stands out due to the greater annual production of tin with respect to that of gallium, indium, and germanium, thus making it an economically viable choice for experimental investigation.

Thanks to the various coordination modes of $\{CuSe_x\}$ units within a ternary Cu/Sn/Se system, we were able to obtain a wide spectrum of products based on diverse copper-selenido stannate subunits. This was achieved by slight variations of the synthetic protocols and afforded single crystals of the new compounds $(C_2C_2Im)_9Li[Cu_{10}Sn_6Se_{22}]$ (**1**), $(C_2C_2Im)_4[Cu_8Sn_6Se_{18}]$ (**2**), $(C_2C_1Im)_3[Cu_5Sn_3Se_{10}]$ (**3**), and $(C_2C_2Im)_5[Cu_8Sn_6Se_{18}F]\cdot(C_2C_2Im)[BF_4]$ (**4**). For comparison, we also synthesized a salt based on a binary selenido stannate network, $\{(C_2C_2Im)_2[Sn_3Se_7]\}_4\cdot\{(C_2C_2Im)[BF_4]\}_2$ (**5**). A thorough analysis of the five compounds illustrates the significance of Cu^+ for structural expansion, narrowing of the optical gap, and enhancement of the photocurrent conversion performance compared to binary selenido stannates.

Scheme 1. Summary of Common Coordination Geometries of Tt^{4+} (Sn^{4+} and Ge^{4+}); Tt^{2+} (Sn^{2+} and Ge^{2+}); Tr^{3+} (Ga^{3+} and In^{3+}); M^{2+} (Zn^{2+}, Cd^{2+}, Mn^{2+}, Fe^{2+}, etc.) and Cu^+ with Ch^{2-} (S^{2-} and Se^{2-}) Observed in Binary or Multinary Chalcogenido Metalate Substructures

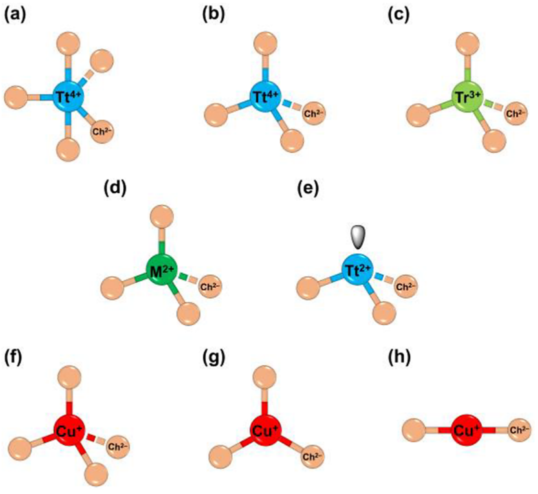

2. METHODS

2.1. General Synthesis Methods

All operations and reactions were performed in an argon atmosphere by using standard Schlenk line or glovebox techniques. The used precursors of $[Li_4(H_2O)_{13}][SnSe_4]$[40] and $[K_4(H_2O)_4][SnSe_4]$[41] were prepared according to literature procedures; 2,6-dimethylmorpholine (DMMP; Sigma-Aldrich, 99.8%) was dried over P_2O_5, distilled and stored over molecular sieve (3 Å); 1,3-diethylimidazolium tetrafluoroborate, $(C_2C_2Im)[BF_4]$, from abcr Gmbh (99%); 1-ethyl-3-methylimidazolium tetrafluoroborate, $(C_2C_1Im)[BF_4]$, from Sigma-Aldrich (99%); and copper(I) iodide from Sigma-Aldrich (98%) were degassed before use. All reactions were carried out with ionothermal approaches, and the synthesis procedures of compounds **1**−**5** are detailed as below.

2.2. Synthesis of $(C_2C_2Im)_9Li[Cu_{10}Sn_6Se_{22}]$ (1)

27 mg of $[Li_4(H_2O)_{13}][SnSe_4]$ (0.039 mmol), 10 mg of CuI (0.053 mmol), 500 mg of $(C_2C_2Im)[BF_4]$ (2.36 mmol), and 100 μL of DMMP (0.812 mmol) were combined in a borosilicate glass ampule, which was flash frozen in a liquid nitrogen filled dewar, evacuated to an internal pressure of 0.05 mbar, and subsequently flame-sealed. After standing in a sand bowl for an hour, the sealed ampule was heated to 120 °C from room temperature at a heating rate of 30 °C/h, kept at 120 °C for 72 h, and then cooled down to room temperature at a cooling rate of 5 °C/h. A few reddish-black, cubic-shaped crystals of **1** were obtained.

2.3. Synthesis of $(C_2C_2Im)_4[Cu_8Sn_6Se_{18}]$ (2)

27 mg of $[K_4(H_2O)_4][SnSe_4]$ (0.040 mmol), 10 mg of CuI (0.053 mmol), 10 mg of LiCl (0.236 mmol), 500 mg of $(C_2C_2Im)[BF_4]$ (2.36 mmol), and 100 μL of DMMP (0.812 mmol) were combined in a borosilicate glass ampule, which was flash frozen in a liquid nitrogen filled dewar, evacuated to an internal pressure of 0.05 mbar, and subsequently flame-sealed. After standing in a sand bowl for an hour, the sealed ampule was heated to 150 °C from room temperature at a heating rate of 30 °C/h, kept at 150 °C for 72 h, and then cooled down to room temperature at a cooling rate of 5 °C/h. Reddish-black, rod-shaped crystals of **2** were obtained in 58% yield (12 mg) with

https://doi.org/10.1021/jacsau.4c00375

respect to $[K_4(H_2O)_4][SnSe_4]$. The crystals were washed with water (~10 mL) three times and treated with methanol (~5 mL) once to remove most of the ionic liquid and then allowed to dry in air. For long-term use, the crystals were stored in an argon-filled glovebox.

2.4. Synthesis of $(C_2C_1Im)_3[Cu_5Sn_3Se_{10}]$ (3a and 3b)

27 mg of $[Li_4(H_2O)_{13}][SnSe_4]$ (0.039 mmol), 10 mg of CuI (0.053 mmol), 500 mg of $(C_2C_1Im)[BF_4]$ (2.53 mmol), and 100 μL of DMMP (0.812 mmol) were combined in a borosilicate glass ampule, which was flash frozen in a liquid nitrogen filled dewar, evacuated to an internal pressure of 0.05 mbar, and subsequently flame-sealed. After standing in a sand bowl for an hour, the sealed ampule was heated to 120 °C from room temperature at a heating rate of 30 °C/h, kept at 120 °C for 72 h, and then cooled down to room temperature at a cooling rate of 5 °C/h. Reddish-black, octahedron-shaped crystals of inseparable **3a** and **3b** were obtained in a 34% yield (8 mg) with respect to $[Li_4(H_2O)_{13}][SnSe_4]$. The crystals were washed with water (~10 mL) three times and treated with methanol (~5 mL) once to remove most of the ionic liquid and then allowed to dry in air. For long-term use, the crystals were stored in an argon-filled glovebox.

2.5. Synthesis of $(C_2C_2Im)_5[Cu_8Sn_6Se_{18}F]\cdot[C_2C_2Im][BF_4]$ (4)

27 mg of $[Li_4(H_2O)_{13}][SnSe_4]$ (0.039 mmol), 10 mg of CuI (0.053 mmol), 500 mg of $(C_2C_2Im)[BF_4]$ (2.36 mmol), and 100 μL of DMMP (0.812 mmol) were combined in a borosilicate glass ampule, which was flash frozen in a liquid nitrogen filled dewar, evacuated to an internal pressure of 0.05 mbar, and subsequently flame-sealed. After standing in a sand bowl for an hour, the sealed ampule was heated to 150 °C from room temperature at a heating rate of 30 °C/h, kept at 150 °C for 72 h, and then cooled down to room temperature at a cooling rate of 5 °C/h. Reddish-black, cubic-shaped crystals of **4** were obtained. However, the yield of **4** was not calculable owing to the cocrystallization of bright red crystals of **5** in this reaction. The crystals were washed with water (~10 mL) three times and treated with methanol (~5 mL) once to remove most of the ionic liquid, and then allowed to dry in air. For long-term use, the crystals were stored in an argon-filled glovebox.

2.6. Synthesis of $(C_2C_2Im)_8[Sn_{12}Se_{28}]\cdot(C_2C_2Im)_2[BF_4]_2$ (5)

27 mg of $[Li_4(H_2O)_{13}][SnSe_4]$ (0.039 mmol), 500 mg of $(C_2C_2Im)[BF_4]$ (2.36 mmol), and 100 μL of DMMP (0.812 mmol) were combined in a borosilicate glass ampule, which was flash frozen in a liquid nitrogen filled dewar, evacuated to an internal pressure of 0.05 mbar, and subsequently flame-sealed. After standing in a sand bowl for an hour, the sealed ampule was heated to 150 °C from room temperature at a heating rate of 30 °C/h, kept at 150 °C for 72 h, and then cooled down to room temperature at a cooling rate of 5 °C/h. Bright red, hexagon-shaped crystals of **5** were obtained in a 35% yield (23 mg) with respect to $[Li_4(H_2O)_{13}][SnSe_4]$. Compound **5** is also a byproduct of the reaction yielding **4** (see Section 2.5). The crystals were washed with water (~10 mL) three times and treated with methanol (~5 mL) once to remove most of the ionic liquid, and then allowed to dry in air. For long-term use, the crystals were stored in an argon-filled glovebox.

2.7. Single-Crystal X-ray Diffraction Studies

Single-crystal diffraction data were collected on a Bruker D8Quest with a CMOS detector (**1**: $T = 100$ K, Mo–Kα radiation, $\lambda = 0.71073$ Å) or an area detector system Stoe StadiVari (**2**–**5**: $T = 100$ K, Cu Kα radiation, $\lambda = 1.54186$ Å). The structures were solved by dual-space methods implemented in SHELXT from SHELXL-2018/13637 and refined by full matrix least-squares methods against F^2 using the SHELXL program.[42] Measurement, structure solution, and refinement results, as well as details on the back Fourier transform procedure using the SQUEEZE algorithm in the PLATON program package,[43,44] are detailed in Tables S1–S6. Crystallographic data for the structures reported in this paper have been deposited with the Cambridge Crystallographic Data Center as supplementary publication no. CCDC-2327171–CCDC-2327176. Copies of the data can be obtained free of charge on application to CCDC (Email: deposit@ccdc.cam.ac.uk).

2.8. Energy-Dispersive X-ray (EDX) Spectroscopy

EDX analyses of single crystals (Figures S21–S25) were carried out using an EDX device Voyager 4.0 of Noran Instruments coupled with an electron microscope CamScan CS 4DV. Data acquisition was performed with an acceleration voltage of 10 or 15 kV and an accumulation time of 100 s.

2.9. Powder X-ray Diffraction (PXRD)

PXRD data of compounds **2**–**5** (Figures S26–S29) were obtained with Cu Kα radiation ($\lambda = 1.54186$ Å) in transmission mode on a Stoe StadiMP diffractometer using a Mythen detector system. The data were examined using WinXPOW.[45]

2.10. Light-Microscopy

Light microscopic investigation of crystals was performed on the stereo light microscope SteREO Discovery.V8 by Carl Zeiss. The microscope was equipped with a high-intensive cold-light source CL 1500 ECO, an Achromat S 0.63x objective (FWD 107 mm), a PL 10*x*/21 Br ocular, and the microscope camera AxioCam MRc 5 with the camera adapter 60N–C 2/3″ 0.63x. The raw photo material was examined by the AxioVision40 × 64 4.9.1 SP1 software.

2.11. Optical Absorption Properties

Optical absorption spectra of compounds 2–5 were measured in diffuse-reflectance mode on single crystals employing a Varian Cary 5000 UV/vis/NIR spectrometer from Agilent, equipped with a Praying Mantis accessory for the solid-state samples. Tauc plots were generated using the Kubelka–Munk function $(F(R\infty)h\nu)^{1/\gamma}$,[46,47] with $\gamma = 0.5$ or 2, indicative for a direct allowed optical gap, or indirect optical gap, respectively (Figure S31).

2.12. Measurement of the Photocurrent

Preparation of crystal-modified carbon cloth working electrodes: 10 mg of crystals of each sample was first ground in a mortar, and subsequently, the obtained powder was ultrasonicated in an ethanol solution containing 0.5% Nafion for one hour. This mixture was added dropwise to the surface of a carbon cloth. The working electrodes were obtained after evaporation of ethanol thereupon, and the effective area was determined to be 0.246 cm^2. Cyclic voltammograms and amperometric response of compounds 2–5 (Figure S32) decorated working electrodes were carried out using a PGU-BI 100 potentiostat (IPS Jaissle). Ag/AgCl in 3 M KCl was used as the reference electrode; a Pt plate was applied as an auxiliary electrode. Ar-saturated 0.1 M phosphate buffer at pH = 7 was used as the electrolyte. The preparation of the working electrode and measurement of cyclic voltammograms are simplified as Scheme S1.

3. RESULTS AND DISCUSSION

3.1. Syntheses

In general, fewer copper-selenido stannates are reported than copper-sufido stannates, typically because of the lower stability of the former and their corresponding intermediates and because of the formation of side products such as CuSe or Cu_2Se during the reaction. Aiming at limiting decomposition on the one hand and inhibition of the reactivity between copper and selenide reagents on the other hand, we herein synthesized the salts $[Li_4(H_2O)_{13}][SnSe_4]$[40] and $[K_4(H_2O)_4][SnSe_4]$ first,[41] and explored their reactivities with CuI under inert conditions by an ionothermal approach. $[SnSe_4]^{4-}$ salts offer a platform to already have Sn–Se bonds preformed before the addition of copper reagents; therefore, the formation of CuSe and Cu_2Se byproducts can be avoided to some extent owing to the lower reactivity between Se^{2-} ligands and Cu^+, but also making it easier to form the target compounds.

As shown in Scheme 2, five new compounds were synthesized by reaction of $[Li_4(H_2O)_{13}][SnSe_4]$ or $[K_4(H_2O)_4][SnSe_4]$ with CuI in the ionic liquids $(C_2C_x\text{Im})$-

Scheme 2. Schematic Illustration of the Syntheses of Compounds 1–5[a]

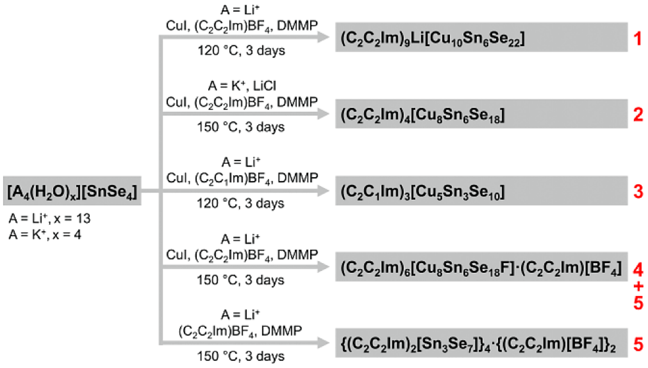

[a] **1** and **3–5** were prepared by the use of $[Li_4(H_2O)_{13}][SnSe_4]$ in ionic liquids; **2** was formed by mixing $[K_4(H_2O)_4][SnSe_4]$ and LiCl salts as starting materials instead. The use of CuI is necessary for the formation of **1–4**, and the DMMP auxiliary is needed for all syntheses.

$[BF_4]$ (x = 2 for **1–2** and **4–5**; x = 1 for **3**) and 2,6-dimethylmorpholine (DMMP) at 120 or 150 °C for 3 days; the role of DMMP is 2-fold: protonation of the base by water from the precursor salts inhibits acidic decomposition of selenido metalates under formation of H_2Se, and H-bonding activity of the ammonium cation is anticipated to help in the formation of the larger network structures.

The reaction of $[Li_4(H_2O)_{13}][SnSe_4]$ and CuI in $(C_2C_2Im)[BF_4]$ and DMMP at 120 °C for 3 days yielded a few reddish-black crystals of the ternary anion of $[Cu_{10}Sn_6Se_{22}]^{10-}$ in **1**, which is stabilized by both $(C_2C_2Im)^+$ and Li^+ counterions. Treatment of $[K_4(H_2O)_4][SnSe_4]$ and LiCl with CuI in the same reaction medium at 150 °C afforded **2** instead (approximately 58% yield; reddish-black crystals); even though neither Li^+/K^+ nor Cl^- were included in the product, their existence apparently affected the solvation behavior of the ionothermal flux and thus led to the formation of a different compound. As has been previously reported, the modification in the length of the alkyl chains of the ionic liquid counterions can effectively modulate the structure of the anionic cluster units obtained from such reactions.[28] By substituting one of the ethyl groups of the cation $(C_2C_2Im)^+$ in $(C_2C_2Im)[BF_4]$ with a methyl group and running the reaction as for the preparation of **1**, we obtained an inseparable mixture of reddish-black crystals comprising **3a** and **3b** (approximately 34% yield in total), which are based on enantiomeric-selenido metalate open-framework structures. Besides the nature of the ionic liquid counterion, the reaction temperature is another significant parameter to modify solubility and thus the crystallization conditions of chalcogenido metalates in ionothermal environments. By raising the reaction temperature from 120 °C for the formation of **1**, to 150 °C, reddish-black cubic crystals of **4** were obtained, yet always along with a (minor) side product. The latter appears as bright red crystals and was identified as compound **5**, which can be obtained as a pure product in approximately 35% yield if CuI is not present in the reaction mixture. It should be noted that the presence of $[BF_4]^-$ anions is essential for the successful synthesis of all compounds. Upon replacement of $[BF_4]^-$ by Br^- or Cl^- anions, none of the named products crystallized. While this is obvious for **4** and **5**, which contain $[BF_4]^-$ anions, it is put down to the contribution of this anion to the sweet spots in polarities and melting points of the corresponding fluxes for all compounds. In addition, using CuI as a copper source turned out to be instrumental for the formation of copper-rich products **1–4**, as no identifiable compounds were observed using CuCl, $CuCl_2$, or $Cu(OAc)_2 \cdot H_2O$. **2**, **4**, and **5** are also isolated from one batch by reacting $[Li_4(H_2O)_{13}][SnSe_4]$ with CuBr at 150 °C, yet with very poor crystal quality due to heavily intergrown crystals. It is assumed that the solvation of Cu^+ and I^- ions and their solution dynamics in ionic liquids exactly meets the requirements for the molecule or network formation and subsequent crystallization, while the other anions cause a too high (Cl^-) or to low (OAc^-) reactivity under the given conditions. The use of bromides, exhibiting a reactivity between Cl^- and I^-, affords crystalline material of significantly lower quality owing to intergrown crystals.

3.2. Crystal Structures

All five compounds formed crystals suitable for X-ray diffraction studies (CCDC 2327171–2327176). Their structures will be described in what follows.

$(C_2C_2Im)_9Li[Cu_{10}Sn_6Se_{22}]$ (**1**) crystallizes in the high symmetrical cubic space group $Pa\bar{3}$ (No. 206) with eight formula units per unit cell (Figure 1a). The asymmetric unit, as shown in Figure S1, contains four copper atoms, two tin atoms, and eight selenium atoms. The relative atomic content was confirmed by means of EDX measurements. As pictured in Figure 1b, the cluster anion in **1** can be viewed as a molecular core–shell structure. The central fragment, $\{Cu_7Se\}$ (Figure 1c), is capped and stabilized by three dimeric $\{Sn_2Se_7\}$ anionic motifs (Figure 1d). Three additional copper atoms serve to bridge the $\{Sn_2Se_7\}$ anions and assemble into a larger trigonal $\{Cu_3Sn_6Se_{21}\}$ shell. The $\{Cu_7Se\}$ core unit adopts a distorted cubane-type architecture. The distances between neighboring copper atoms range from 2.598(1) Å to 2.912(1) Å, which are longer than the interatomic distance in metallic copper (2.56 Å);[48] therefore, the bonding interactions between Cu atoms in **1** are negligible; the dashed lines drawn between them in Figure 1c only serve to clearly demonstrate their arrangement. Nine of the copper atoms adopt trigonal-planar coordination modes, and the remaining central, tetracoordinated Cu atom serves to bridge three capping $\{Sn_2Se_7\}$ motifs and the remaining selenium atom of the anionic cluster (Figure S2). The $[Cu_{10}Sn_6Se_{22}]^{10-}$ anion we present here has a larger cluster size (Figures 1b and S4d) and significantly higher charge, as compared to the reported $[M_7As_3Ch_{13}]^{4-}$ (Figures 1e and S4e,f; M = Cu or Ag, Ch = Se or Te) molecules.[49,50]

These observations can be attributed to the successful incorporation of Sn atoms into the cluster anion. The local negative charges of the $\{Sn_2Se_7\}$ capping units in **1** are 6−(cf. the 3− charge of $\{AsSe_4\}$ in $\{M_7As_3Ch_{13}\}$), which goes hand in hand with the introduction of more tricoordinated Cu atoms to balance a part of their negative charges and hence stabilize the cluster. Thereby, the cluster size increases from 9.11 to 9.95 Å in the $[M_7As_3Ch_{13}]^{4-}$ anions to 13.84 Å in the $[Cu_{10}Sn_6Se_{22}]^{10-}$ anion in **1**.

$(C_2C_2Im)_4[Cu_8Sn_6Se_{18}]$ (**2**) crystallizes in the monoclinic crystal system, space group $P2_1/c$, (No. 14). As illustrated in Figure 2a, eight crystallographically independent copper atoms, six tin atoms, and 18 selenium atoms form the unprecedented anionic substructure of the asymmetric unit in **2**. The valence state of all copper atoms, which are found in trigonal-planar or tetrahedral coordination modes (Figure S5), is assigned as +1 for charge balance, as further demonstrated by bond valence

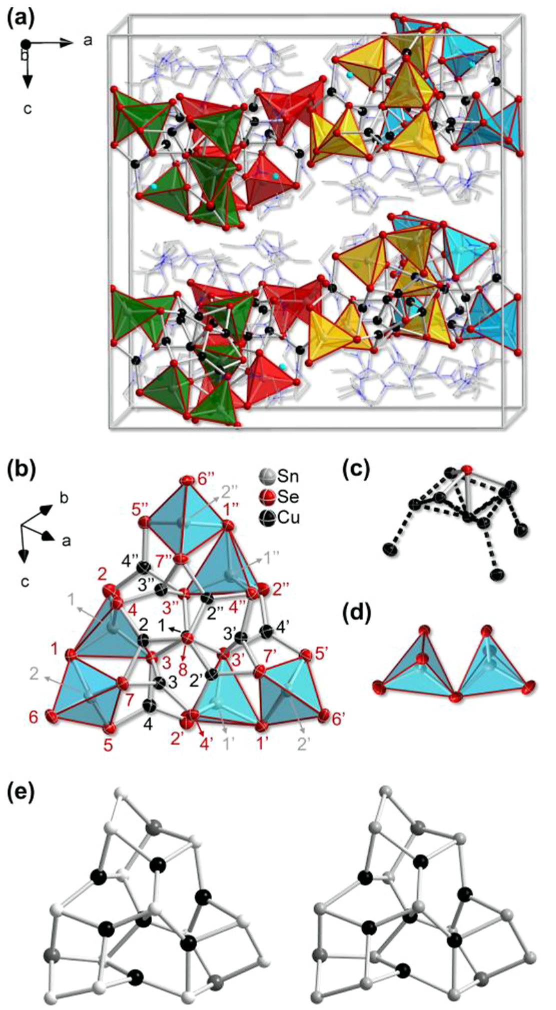

Figure 1. Illustration of the crystal structure of **1**. View of the unit cell of **1**. Ionic liquid cations are shown in wire mode; H atoms are omitted. For clarity, the $\{Sn_2Se_7\}$ units of different $[Cu_{10}Sn_6Se_{22}]^{10-}$ cluster anions are shown in polyhedral mode with different colors (a). Molecular structure of the $[Cu_{10}Sn_6Se_{22}]^{10-}$ cluster anion in **1**; atom numbers are given in the color code indicated for the atom types (b). The $\{Cu_{10}Se\}$ core of $[Cu_{10}Sn_6Se_{22}]^{10-}$ (c). Dimeric $\{Sn_2Se_7\}$ capping motif in $[Cu_{10}Sn_6Se_{22}]^{10-}$ (d). Thermal ellipsoids are drawn at the 50% probability level in Figure 1b–d. Structures of reported cluster anions $[Cu_7As_3Se_{13}]^{4-}$ (left) and $[Cu_7As_3Te_{13}]^{4-}$ (right) for comparison; gray shade of atoms: Cu—black, As—dark gray (70%), Te—gray (40%), and Se—light gray (10%) (e). See the Supporting Information for further structural details.

sum (BVS) calculations (Table S8). The distances between neighboring copper atoms lie in the range 2.6176(2)–3.1850(2) Å, which showcase the negligible Cu···Cu bonding interactions. In terms of reticular chemistry,[51] two crystallographically independent $\{Cu_4Sn_2Se_6\}$ units represent the repeating motifs that are extended into a backbone-type strand and bridged by a $\{Sn_2Se_6\}$ substructure to be further assembled into a two-dimensional polymeric structure (Figure 2b); the architecture of the layers accords with an ***hcb*** net upon regarding each of the repeating units as a node. As displayed in Figure 2c, two parallel anionic wave-shaped layers arranged in the crystal structure of **2**. Notably (and rarely) all of the ionic liquid cations could be localized in the crystal structure. Three quarters of them serve to separate the anionic components, situated between the interlayers of the neighboring substructures. The remaining quarter of them were found within the six-membered rings of each single layer (Figure 2d) for further charge compensation and internal stabilization of the anionic architecture. More structural details are given in the Supporting Information (Figures S6–S9).

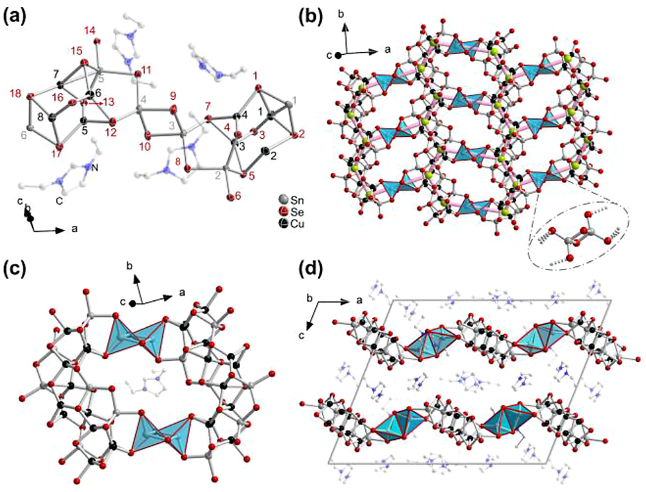

Figure 2. Asymmetric unit of **2** with the labeling scheme. Thermal ellipsoids are drawn at 50% probability level. A corresponding color code was used for the atom labels (a). View of the two-dimensional anionic substructure of **2**. Counterions are omitted for clarity. The simplified ***hcb*** net that is obtained when each repeating unit is regarded as a node (displayed as a lime sphere) is highlighted by sticks of rose color. The bridging $\{Sn_2Se_6\}$ units are highlighted in polyhedral mode, and one of them is shown in bond and stick mode for clarity (b). Illustration of the cyclic substructure in the (distorted) honeycomb-like 2D network including one counterion (c). Side view of the corrugated 2D layers and the counterions in between them (d). See the Supporting Information for further structural details.

$(C_2C_1Im)_3[Cu_5Sn_3Se_{10}]$ (**3**) crystallizes as a mixture of enantiomerically pure crystals, denoted as compounds **3a** and **3b**, in the trigonal crystal system in the two corresponding chiral space groups $P3_2$ (No. 145) and $P3_1$ (No. 144), respectively. As displayed in Figure S10, the asymmetric units of **3a** and **3b** contain five copper atoms, three tin atoms, and ten selenium atoms (the Cu5 positions of both being split into Cu5A and Cu5B due to heavy disorder). The oxidation state of all copper atoms was assigned as +1 according to their trigonal-planar coordination geometry (Figure S11) and as confirmed by BVS calculations (Tables S9 and S10). As depicted in Figure 3a, the repeat units of **3a** and **3b** are connected to identical units via sharing tin atoms at four corners of the building blocks (Figure 3b,c) and further assemble into chiral quartz (***qtz***) networks (Figures 3d,e and S12). Apart from the inverted chirality, compounds **3a** and **3b** possess the same anionic structures and are templated by the same counterions. The networks of **3a** and **3b** feature two different types of chirality: the naturally chiral ***qtz*** net and the one-dimensional chirality of the helix (Figure 3f,g). Most recently, similar compounds of both enantiomers, **COC-10-L** and **COC-10-D** with the formula of $(H^+{-}DBN)_3[Cu_5Sn_3Se_{10}]$ (DBN = 1,5-diazabicyclo[4.3.0]non-5-ene),[52] have been obtained through solvothermal reactions, with the difference being the chiral space groups of $P6_4$ and $P6_2$ in **COC-10-L** and **COC-10-D**. We reason that the use of different structure directing agents, $(C_2C_1Im)^+$ for **3a** and **3b**, $(H^+{-}DBN)$ for **COC-10-L** and **COC-10-D**, led to the formation of the same anionic

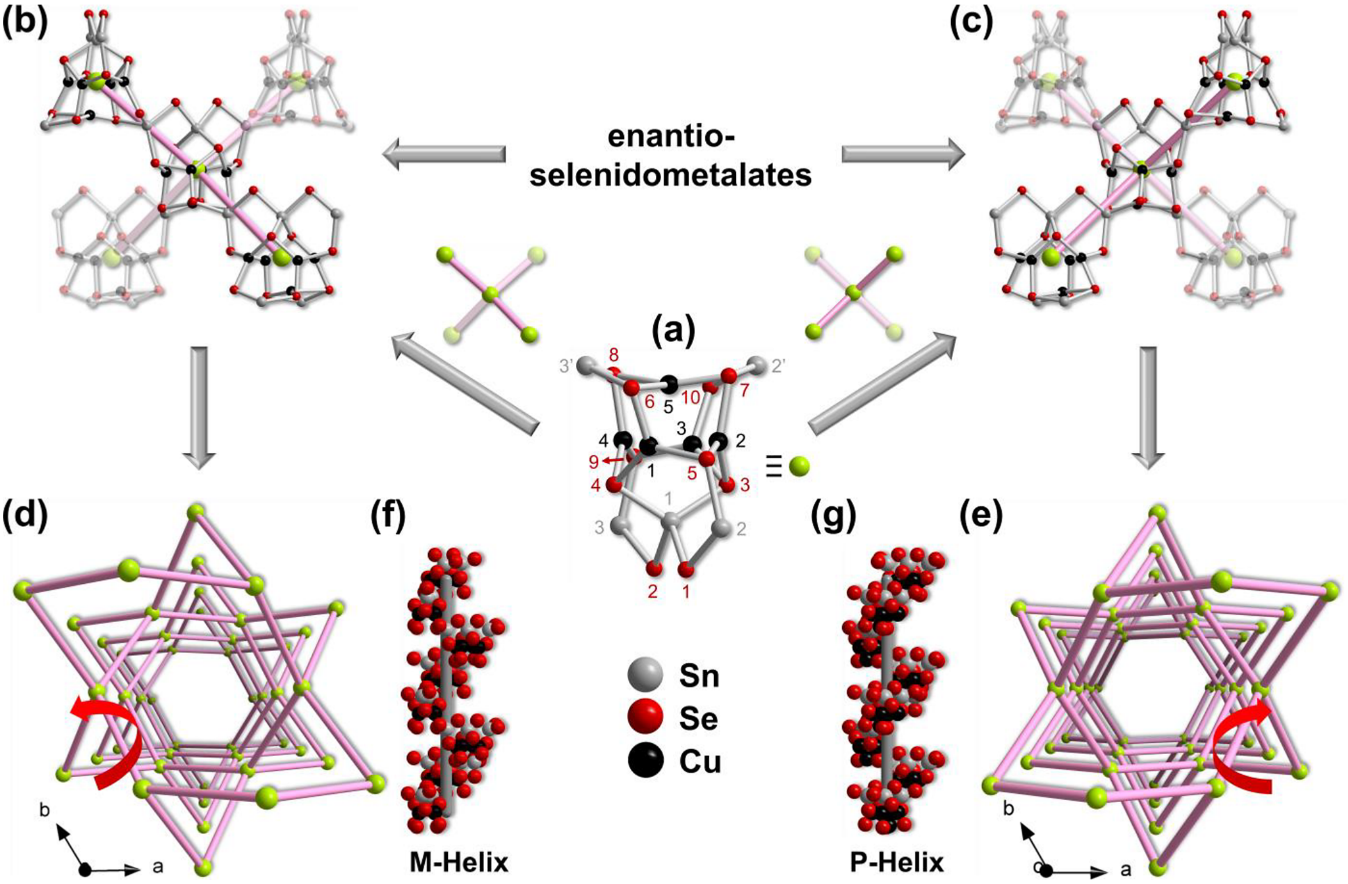

Figure 3. Structure of one secondary building unit in **3a** and **3b**, shown for **3a** as an example; a corresponding color code was used for the atom labels (a). Illustration of the enantiomeric linking mode between the second building units in **3a** (b) and **3b** (c), highlighted with increasing transparency as the units become more distant from the viewpoint of the viewer. Illustration of the simplified chiral ***qtz*** net of **3a** (d) and **3b** (e) upon treatment of each building block as a node. The M-helix is observed along axis *c* in **3a** (f). The P-helix observed along axis *c* in **3b** (g). See the Supporting Information for further structural details.

frameworks but with altered chiral space groups, underpinning the notable influence of the reaction medium and the cations originating from it on the stereochemistry during product formation. Owing to heavy disorder of the ionic liquid counterions that are located at the solvent-accessible spaces (Figure S13), we were not able to localize them on the difference Fourier map; to avoid impairment of the refinement, the corresponding electron density was detracted from the data by the back-Fourier-transform method.[53] The formulas of **3a** and **3b** were determined to be $(C_2C_1Im)_3[Cu_5Sn_3Se_{10}]$ based on the single-crystal X-ray diffraction (SC-XRD) measurements and charge balance rules.

$(C_2C_2Im)_5[Cu_8Sn_6Se_{18}F]\cdot(C_2C_2Im)[BF_4]$ (**4**) crystallizes in the highly symmetric cubic space group of $Pm\overline{3}$ (No. 200) with one $\{FCu_8Sn_6Se_{12}Se_{12\times(1/2)}\}$ building block in the unit cell (Figure 4a). Notably, the Cu:Sn:Se ratio of **4** is the same as that for **2**, highlighting the key structure-directing role of the additional F^- ion and the impact of the slightly varied reaction conditions for product formation. The core of the building unit comprises a cubic array of copper atoms with the neighboring Cu···Cu distances being 3.3241(6) Å and correspondingly with no obvious interactions between adjacent copper atoms (Figure 4b). The $\{Cu_8\}$ cube accommodates a F^- anion, which originated from the anion of the ionic liquid $(C_2C_1Im)[BF_4]$; its presence was further confirmed by EDX analysis. Twelve selenium atoms surround the core motif by bridging each edge of the $\{FCu_8\}$ cube to form an icosahedral $\{FCu_8Se_{12}\}$ cluster unit. Bridging of the latter in compound **4** by six $\{Sn_2Se_2\}$ units affords a three-dimensional ***pcu*** network (Figure 4b−d). It is noteworthy that although $\{Cu_8Ch_m\}$ (Ch = S, Se; *m* = 12, 13) clusters have been reported (Figure S16b−d), this is the first observation on the inclusion of F^- in $\{Cu_8\}$ cubes that are assembled in a network structure. Compared to the known molecular cages of clusters $[Cu_8(F)\{Se_2P(O^iPr)_2\}_6]$ and $[Cu_8(S)\{Se_2P(O^iPr)_2\}_6]^-$ (Figure S16e,f),[54] compound **4** features slightly longer Cu···Cu and Cu···F distances. We attribute the volume expansion of the building unit, which is observed in the extended framework, to the lack of terminal ligands and, thus, larger average coordination numbers of the involved atoms.

A replacement of $[BF_4]^-$ anions of ionic liquids with Cl^- or Br^- did not allow for the formation of the same compound. This demonstrates that $(C_2C_2Im)[BF_4]$ not only acts as solvent and template for the ionothermal reactions but is noninnocent and actively involved in the bottom-up construction of the cluster units. We assume that the $\{Cu_8\}$ cube is not capable of accommodating anions larger than F^-. As shown in Figure S17, a disordered $[BF_4]^-$ anion, originating from the ionic liquid, could be identified at the corner of each unit cell, which further supports the important role of $(C_2C_2Im)[BF_4]$ as the reaction medium. Heavy disorder of the cations allowed for the high overall symmetry of the crystal

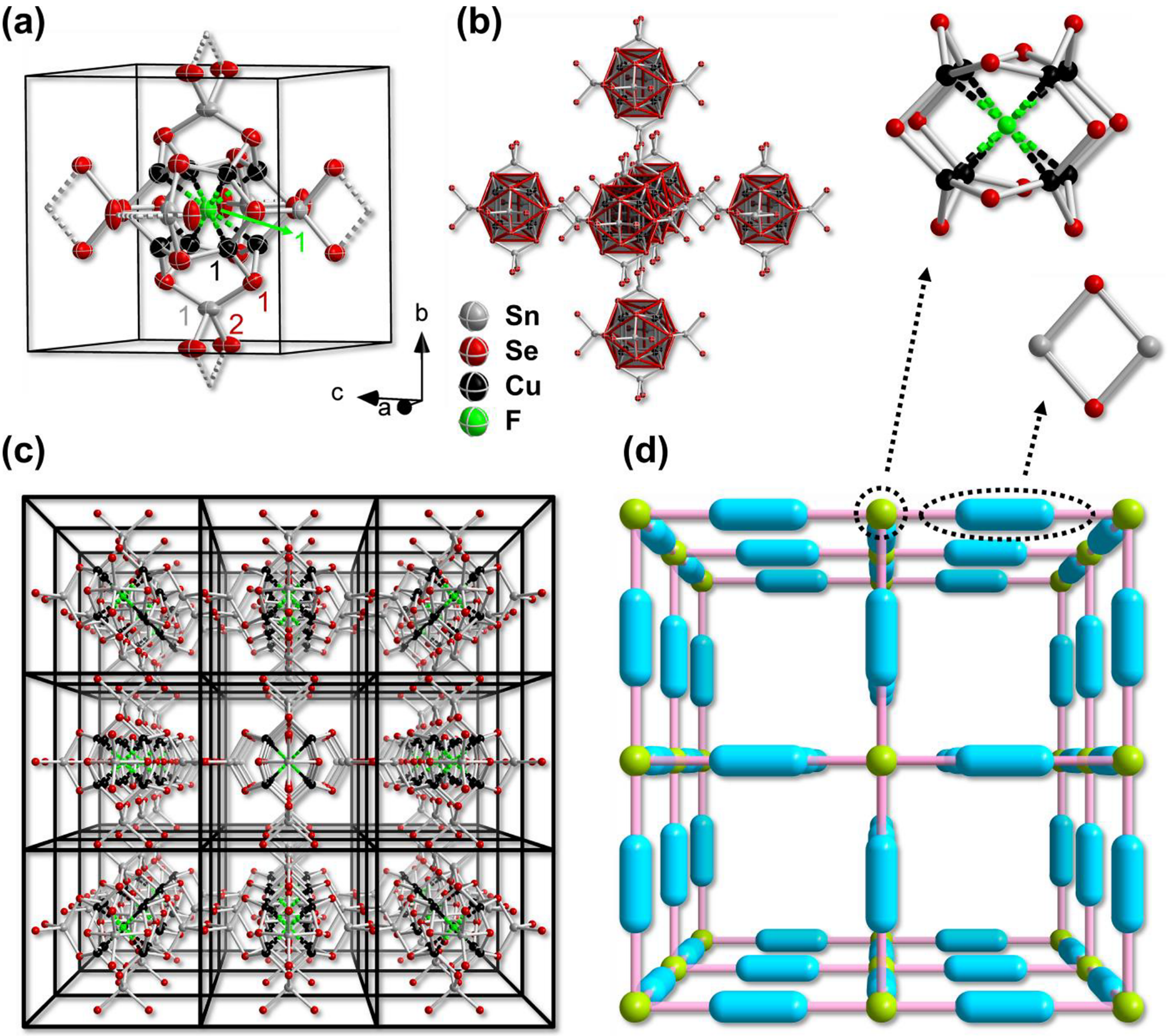

Figure 4. Structure of the building units in the unit cell in **4**. Thermal ellipsoids are drawn at 50% probability level. A corresponding color code was used for the atom labels (a). Illustration of the linkage of building units $\{FCu_8Se_{12}\}$ and $\{Sn_2Se_2\}$ in **4** (b). Extension of the anionic substructure in a 3 × 3 × 3 supercell (c). The simplified ***pcu*** net of **4** was obtained upon treating each $\{FCu_8Se_{12}\}$ motif as a node and each $\{Sn_2Se_2\}$ unit as a linker. The disordered $[BF_4]^-$ anions have been omitted for clarity (d). See the Supporting Information for further structural details.

structure, as they just appear as smeared electron density that does not allow for the localization on the difference Fourier map. Correspondingly, the SQUEEZE routine was applied to account for this feature—as typical for many structures of this kind.[53] The solvent accessible voids illustrated in Figure S18 are in accordance with the accommodation of a total of six $(C_2C_2Im)^+$ cations per unit cell within the crystal structure of **4**.

$\{(C_2C_2Im)_2[Sn_3Se_7]\}_4\cdot\{(C_2C_2Im)[BF_4]\}_2$ (**5**) crystallizes in the triclinic space group $P\overline{1}$ (No. 2) with a unit cell volume of 6667 Å^3. In the asymmetric unit, the anionic selenido stannate substructure contains 12 crystallographically independent tin atoms and 28 selenium atoms, which are further surrounded by ten $(C_2C_2Im)^+$ cations and two $[BF_4]^-$ anions (see Figure S19). The well-known honeycomb-like 2D layer is formed by repeating the $\{Sn_3Se_7\}$ unit via corner sharing of μ-Se atoms (Figure 5a,b). Two of the $(C_2C_2Im)^+$ cations are located inside the hexagonal pores of the layer, six of them are intercalated in between the adjacent layers, and the remaining two cations balance the charges of two $[BF_4]^-$ anions within the crystal structure (Figures S19 and S20). There is no interaction between the anionic substructures and the $[BF_4]^-$ anions; therefore, this compound can be regarded as a double salt. In addition to being a side product during the synthesis of compound **4**, compound **5** can also be obtained as a pure product in the absence of CuI, as confirmed by PXRD of the solid product (Figures S28 and S29).

We would like to emphasize that honeycomb-like binary substructures, similar to the one found in **5**, represent the most frequently observed structural motif in chalcogenido stannates obtained under mild (solvothermal or ionothermal) reaction conditions—even in the presence of different structure-directing agents.[55−59] Changing the reaction temperatures or

https://doi.org/10.1021/jacsau.4c00375
JACS Au XXXX, XXX, XXX−XXX

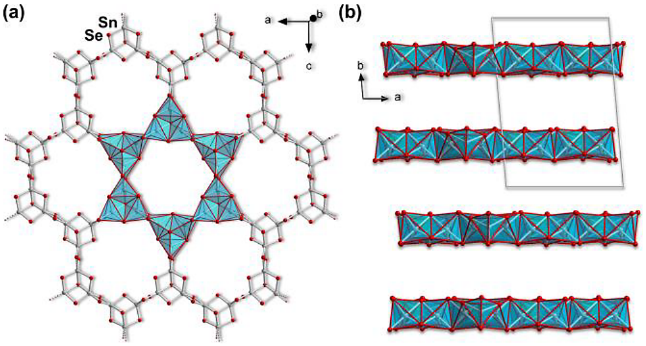

Figure 5. Top view of the two-dimensional, honeycomb-like anionic substructure of **5**, highlighting the six-membered-ring motif in the polyhedral mode (a). Side view of stacking of the layers along the *b* axis in the crystal structure of **5**. Organic cations and $[BF_4]^-$ anions are omitted for the sake of clarity (b). See the Supporting Information for further structural details.

the crystallization conditions allows for access to other motifs, but the variations are still limited. In contrast, the addition of Cu^+ to the reaction system provides huge opportunities for structural variations owing to the cation's diverse coordination modes with chalcogen ligands, which allows for the formation of unprecedented anionic substructures, such as the ones observed for **1**−**4** upon subtle modifications of reaction temperatures, precursor salts, as well as the use of different ionic liquid cations. This way, the spectrum of selenido stannate-based materials experiences a significant structural expansion in spite of relatively similar atomic ratios of the involved elements Cu:Sn:Se of 10:6:22 (**1**), 8:6:18 = 10:7.5:22.5 (**2** and **4**), and 5:3:10 = 10:6:20 (**3**).

3.3. Optical Absorption Properties

Beside the structural expansion of such cluster assemblies, the introduction of Cu^+ was undertaken to modulate the electronic structures of the corresponding compounds. As depicted in Figure 6a−c, solid-state UV−vis diffuse-reflectance spectra were collected on crystalline samples of **2**−**5** and served to calculate the optical gaps of these materials (the investigation of **1** was hampered by the small yield).

It was found that all compounds, in particular **2**−**4**, are narrow band gap semiconductors with E_{gap} values similar to those of reported copper-rich cluster-based materials (1.19−2.50 eV)[39,60−62] and those of the photovoltaic materials Cu_2SnCh_3 and $Cu_2ZnSnCh_4$ (Ch = S, Se; E_{gap} = 1.33−1.88 eV)[63−65] (Table S12).

According to the corresponding Tauc plots shown in Figure S31, the optical band gap energies E_{gap} of **2**−**5** were determined to be 1.39 eV (**2**), 1.75 eV (**3**), 1.83 eV (**4**), and 2.05 eV (**5**), respectively (Figure 6d). In comparison to the E_{gap} of **5**, a distinct redshift of the UV−vis spectra of **2**−**4** is observed upon the introduction of Cu^+ into the reaction system owing to the lower electronic excitation energy of copper(I) selenide (0.50 eV)[66] as compared to tin(IV) selenide (1.07 eV),[67] which also affects the confined structural units present in the title compounds.

Considering the ratios of "$SnSe_2$:Cu_2Se:Se^{2-}" comprised in the four Cu/Sn/Se substructures (normalized to $6SnSe_2$), hence $6SnSe_2$:$5Cu_2Se$:$5Se^{2-}$ in **1**, $6SnSe_2$:$4Cu_2Se$:$2Se^{2-}$ in **2** and **4**, and $6SnSe_2$:$5Cu_2Se$:$3Se^{2-}$ in **3** (cf. $6SnSe_2$:$2Se^{2-}$ in **5**), we do see similar degrees of "Cu_2Se admixtures" relative to $SnSe_2$ in the new compounds **1** − **4**. This explains the similar

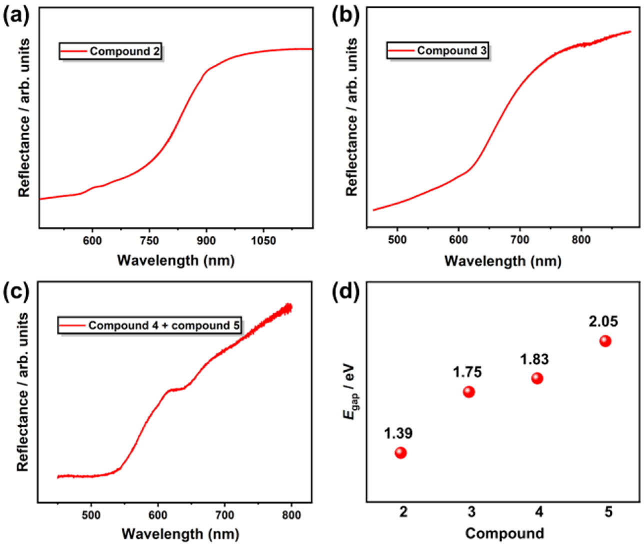

Figure 6. Solid-state UV−vis diffuse-reflectance spectra of **2**, **3**, and **4** plus **5** (a−c). Comparison of the differences between the optical band gap energies E_{gap} of **2**−**5** (d). The Tauc plots derived from the solid-state UV−vis diffuse-reflectance spectra are shown in Figure S31; they were generated using the Kubelka−Munk function $(F(R\infty)h\nu)^{1/\gamma}$, with γ = 2, indicative of an indirect optical gap. A corresponding measurement of **1** was hampered by its small yield.

effect observed for **4** (1.83 eV) and **3** (1.75 eV) as compared to **5** (2.05 eV). We attribute the additional narrowing of the bandgap measured for **2** (1.39 eV), in spite of a slightly lower relative "Cu_2Se content", to a denser anionic substructure—hence supporting the concerted effect on structures and electronic properties by incorporation of Cu^+.

These findings indicate that the synthetic access reported herein provides a straightforward and sustainable way of generating novel semiconductor materials with finely tunable geometric and electronic structures.

3.4. Photocurrent Measurement

Based on the distinct redshift of the optical absorption energies of the compounds comprising Cu^+ ions as compared to the Cu^+-free product, we suspected that we could also find a corresponding effect on the photocurrent conversion efficiencies. Cyclic voltammograms (CV) were recorded on pulverized crystals of **2**, **3**, **4** (with small amounts of side product **5**), or **5** deposited on carbon cloth under white-light irradiation and under the exclusion of light (the corresponding characterization of **1** was hampered by its small yield). To ensure the accuracy of experimental results, the CVs were measured under dark conditions first. As shown in Figure 7a−c, electrodes fabricated with **2**, **3**, and **4** (plus **5**) present nearly two times the current densities during irradiation than those in the dark over the applied potential range (*E*). The photocurrent density of the electrode fabricated with **5** (Figure 7d) indicates that the photocurrent is only about 1.2 times the dark current, which indicates that copper-free selenido stannate improves the photocurrent conversion efficiency under the same irradiation conditions, but at a relative moderate efficiency in comparison to the behavior of the copper-selenido stannates. Also, in terms of the absolute photocurrent and dark current density, electrodes functionalized with the Cu^+-containing materials **2**−**4** exhibit a superior conversion performance than electrodes fabricated with **5**, which we attribute to the faster electron−hole separation during white-light irradiation of the former

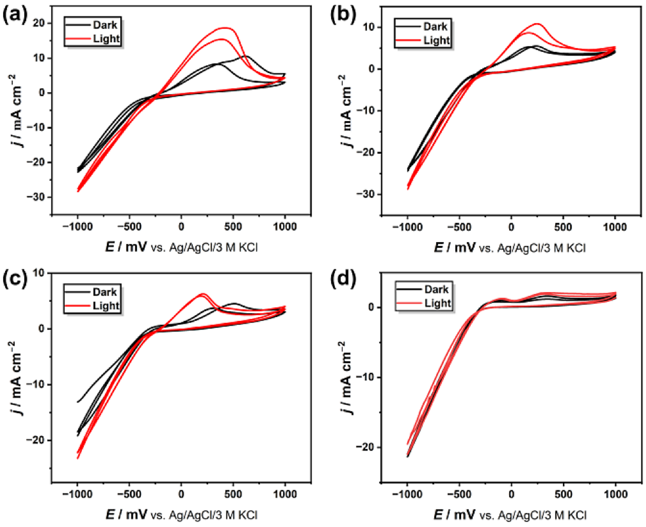

Figure 7. Photocurrent measurements of **2** (a), **3** (b), **4** (with small amounts of side product **5**; c), and **5** (d), given as cyclic voltammograms (CV) of pulverized crystals deposited on carbon cloth. Red curves represent measurements under white-light irradiation. Black curves were recorded under the exclusion of light. Scan rate: 10 mV/s. An Ar-saturated phosphate buffer (c = 0.1 M) at pH = 7 was used as electrolyte, the electrode area was 0.246 cm^2. See the Supporting Information for further details.

three relative to the latter. In addition, the transient photocurrents of all electrodes were studied at a potential E of 250 mV vs Ag/AgCl/3 M KCl to amplify the differences in terms of their densities. As displayed in Figure S32, the compound **5** modified electrode showcases almost negligible photocurrent response properties, while the electrode deposited with **2** achieves excellent current densities of over 20 μA/cm^2. Given the fact that the photocurrent and dark current keep decreasing owing to the moderate stability of these compounds, the photocurrent densities of electrodes decorated with **3** or a mixture of **4** and **5** cannot be calculated. However, we observed the increment of photocurrent in the first 30s after illumination of the sample.

The study demonstrates that introducing Cu$^+$ into selenido stannates allows for an increased photocurrent. The CVs also indicate that only oxidation peaks (Cu$^+$ to Cu^{2+}) occur in the measured cyclic voltammograms of **2**−**4**, indicating that the redox reactions are irreversible and lead to the degradation of the material under the given conditions. In order to improve the redox stability of such cluster-based materials, we aim at an in situ anchoring of Cu^{2+} complexes around Cu$^+$ in our ongoing materials development strategies.

4. CONCLUSIONS

In this work, we contribute to the structural expansion of selenido stannates by introducing Cu$^+$ into the compounds. By reacting the salts $[A_4(H_2O)_x][SnSe_4]$ (A = Li$^+$, x = 13; A = K$^+$, x = 4) with CuI in ionic liquids $(C_2C_2Im)[BF_4]$ or $(C_2C_1Im)[BF_4]$, we were able to access a series of Cu$^+$-containing anionic substructures, ranging from 0D-$\{[Cu_{10}Sn_6Se_{22}]^{10-}\}$ in **1** to 2D-$\{[Cu_8Sn_6Se_{18}]^{4-}\}$ in **2**, 3D-$\{[Cu_5Sn_3Se_{10}]^{3-}\}$ in **3**, and 3D-$\{[Cu_8Sn_6Se_{18}F]^{5-}\}$ in **4**. Compound **1** demonstrates that our approach is suitable to push the size limit of this type of cluster, previously from 23 atoms in related ternary Cu/As/Ch assemblies (Ch = Se or Te) to 38 atoms in the Cu/Sn/Se combination. In compound **2**, we observe an unprecedented 2D network which—like **1**—has not been accessible by traditional synthetic approaches. Compound **3** serves to underpin the influence of reaction media that ultimately provide cations on product formation, including the stereochemistry of complex 3D frameworks. With the observation of compound **4**, we finally expand the $\{FCu_8Ch_{12}\}$ cluster family from a molecular structure to an unprecedented 3D network—again inaccessible by traditional routes—with a concomitant consequence on the optical properties. With the formation of a fifth product, we finally underscore the importance of Cu$^+$ in enriching the family members of selenido metalates: in the absence of Cu$^+$ cations, yet under otherwise unchanged reaction conditions, we obtain compound **5** that is based on binary 2D-$\{[Sn_3Se_7]^{2-}\}$ layers.

Owing to the lower electronic transition energy of Cu$^+$, its inclusion into the anionic substructures not only allows to expand the structures but additionally and simultaneously serves to narrow the optical gaps of corresponding ternary compounds in comparison to those of binary ones as revealed by UV−vis spectroscopy. The excellent light-absorption capabilities therefore served to notably improve the photocurrent conversion efficiencies of such copper-selenido metalates.

In future investigations, we will move on to the structural expansion of other chalcogenido metalates, like the related family of selenido germanates or homologous and mixed chalcogenides, utilizing this successful and straightforward strategy.

■ ASSOCIATED CONTENT

Supporting Information

The Supporting Information is available free of charge at https://pubs.acs.org/doi/10.1021/jacsau.4c00375.

> Experiment details, single-crystal X-ray diffraction (SCXRD) data, supplementary crystallographic figures, powder X-ray diffraction (PXRD) data, light-microscopic images of the single crystals, energy-dispersive X-ray (EDX) spectroscopy, optical absorption spectroscopy, and time-dependent photocurrent measurement (PDF)

■ AUTHOR INFORMATION

Corresponding Author

Stefanie Dehnen − *Institute of Nanotechnology (INT) and Karlsruhe Nano Micro Facility (KNMFi), Karlsruhe Institute of Technology (KIT), 76131 Karlsruhe, Germany;* orcid.org/0000-0002-1325-9228; Email: stefanie.dehnen@kit.edu

Authors

Zhou Wu − *Institute of Nanotechnology (INT) and Karlsruhe Nano Micro Facility (KNMFi), Karlsruhe Institute of Technology (KIT), 76131 Karlsruhe, Germany*

Benjamin Peerless − *Institute of Nanotechnology (INT) and Karlsruhe Nano Micro Facility (KNMFi), Karlsruhe Institute of Technology (KIT), 76131 Karlsruhe, Germany*

Panpan Wang − *Analytical Chemistry—Center for Electrochemical Sciences (CES), Faculty of Chemistry and Biochemistry, Ruhr University Bochum, 44780 Bochum, Germany*

Wolfgang Schuhmann − *Analytical Chemistry—Center for Electrochemical Sciences (CES), Faculty of Chemistry and*

Biochemistry, Ruhr University Bochum, 44780 Bochum, Germany; orcid.org/0000-0003-2916-5223

Complete contact information is available at:
https://pubs.acs.org/10.1021/jacsau.4c00375

Author Contributions

The manuscript was written through contributions of all authors. CRediT: **Zhou Wu** conceptualization, data curation, formal analysis, investigation, validation, writing-original draft, writing-review & editing; **Benjamin Peerless** project administration, validation, writing-review & editing; **Panpan Wang** investigation, validation, visualization, writing-review & editing; **Wolfgang Schuhmann** supervision, validation, writing-review & editing; **Stefanie Dehnen** conceptualization, funding acquisition, resources, supervision, validation, visualization, writing-review & editing.

Notes

The authors declare no competing financial interest.

■ ACKNOWLEDGMENTS

The work was financially supported by the German Research Foundation (Deutsche Forschungsgemeinschaft, DFG). Z.W. acknowledges a PhD fellowship by China Scholarship Council (CSC no. 202006920030). The authors gratefully acknowledge the support by the Karlsruhe Nano Micro Facility (KNMFi).

■ REFERENCES

(1) Su, L.; Wang, D.; Wang, S.; Qin, B.; Wang, Y.; Qin, Y.; Jin, Y.; Chang, C.; Zhao, L.-D. High Thermoelectric Performance Realized through Manipulating Layered Phonon-Electron Decoupling. *Science* **2022**, *375*, 1385−1389.

(2) Zhou, C.; Lee, Y. K.; Yu, Y.; Byun, S.; Luo, Z.-Z.; Lee, H.; Ge, B.; Lee, Y.-L.; Chen, X.; Lee, J. Y.; Cojocaru-Mirédin, O.; Chang, H.; Im, J.; Cho, S.-P.; Wuttig, M.; Dravid, V. P.; Kanatzidis, M. G.; Chung, I. Polycrystalline SnSe with a Thermoelectric Figure of Merit Greater than the Single Crystal. *Nat. Mater.* **2021**, *20*, 1378−1384.

(3) Qin, B.; Wang, D.; Hong, T.; Wang, Y.; Liu, D.; Wang, Z.; Gao, X.; Ge, Z.-H.; Zhao, L.-D. High Thermoelectric Efficiency Realized in SnSe Crystals via Structural Modulation. *Nat. Commun.* **2023**, *14*, 1366.

(4) Zhan, S.; Hong, T.; Qin, B.; Zhu, Y.; Feng, X.; Su, L.; Shi, H.; Liang, H.; Zhang, Q.; Gao, X.; Ge, Z.-H.; Zheng, L.; Wang, D.; Zhao, L.-D. Realizing High-Ranged Thermoelectric Performance in $PbSnS_2$ Crystals. *Nat. Commun.* **2022**, *13*, 5937.

(5) Wang, T.; Duan, X.; Zhang, H.; Ma, J.; Zhu, H.; Qian, X.; Yang, J.-Y.; Liu, T.-H.; Yang, R. Origins of Three-Dimensional Charge and Two-Dimensional Phonon Transports in Pnma Phase $PbSnSe_2$ Thermoelectric Crystal. *InfoMat* **2023**, *5*, No. e12481.

(6) Mannu, R.; Basak, A.; Singh, U. P. Impact of Annealing Time on Copper Tin Selenide Thin Film for UV Sensing Application. *J. Mater. Sci. Mater. Electron.* **2023**, *34*, 2100.

(7) Lokhande, A. C.; Babar, P. T.; Karade, V. C.; Gang, M. G.; Lokhande, V. C.; Lokhande, C. D.; Kim, J. H. The Versatility of Copper Tin Sulfide. *J. Mater. Chem. A* **2019**, *7*, 17118−17182.

(8) Ritchie, C.; Chesman, A. S. R.; Jasieniak, J.; Mulvaney, P. Aqueous Synthesis of $Cu_2ZnSnSe_4$ Nanocrystals. *Chem. Mater.* **2019**, *31*, 2138−2150.

(9) Yan, C.; Huang, J.; Sun, K.; Johnston, S.; Zhang, Y.; Sun, H.; Pu, A.; He, M.; Liu, F.; Eder, K.; Yang, L.; Cairney, J. M.; Ekins-Daukes, N. J.; Hameiri, Z.; Stride, J. A.; Chen, S.; Green, M. A.; Hao, X. Cu_2ZnSnS_4 Solar Cells with over 10% Power Conversion Efficiency Enabled by Heterojunction Heat Treatment. *Nat. Energy* **2018**, *3*, 764−772.

(10) Sahoo, G. S.; Verma, M.; Routray, S.; Mishra, G. P. Unveiling the Effect of CZTSSe Quantum Superlattice on the Interfacial and Optical Properties of CZTS Kesterite Solar Cell. *IEEE Trans. Nanotechnol.* **2024**, 1−8.

(11) Nowak, D.; Atlan, F.; Pareek, D.; Guc, M.; Perez-Rodriguez, A.; Izquierdo-Roca, V.; Gütay, L. Influence of the Precursor Composition on the Resulting Absorber Properties and Defect Concentration in $Cu_2ZnSnSe_4$ Absorbers. *Sol. Energy Mater. Sol. Cells* **2023**, *256*, No. 112342.

(12) Scragg, J. J.; Dale, P. J.; Peter, L. M.; Zoppi, G.; Forbes, I. New Routes to Sustainable Photovoltaics: Evaluation of Cu_2ZnSnS_4 as an Alternative Absorber Material. *Phys. status solidi* **2008**, *245*, 1772−1778.

(13) Das, A.; Kumar, A.; Banerji, P. First Principles Study of Electronic Structure and Thermoelectric Transport in Tin Selenide and Phase Separated Tin Selenide−Copper Selenide Alloy. *J. Phys.: Condens. Matter* **2020**, *32*, 265501.

(14) Feng, M.-L.; Sarma, D.; Qi, X.-H.; Du, K.-Z.; Huang, X.-Y.; Kanatzidis, M. G. Efficient Removal and Recovery of Uranium by a Layered Organic−Inorganic Hybrid Thiostannate. *J. Am. Chem. Soc.* **2016**, *138*, 12578−12585.

(15) Manos, M. J.; Kanatzidis, M. G. Layered Metal Sulfides Capture Uranium from Seawater. *J. Am. Chem. Soc.* **2012**, *134*, 16441−16446.

(16) Wu, T.; Bu, X.; Zhao, X.; Khazhakyan, R.; Feng, P. Phase Selection and Site-Selective Distribution by Tin and Sulfur in Supertetrahedral Zinc Gallium Selenides. *J. Am. Chem. Soc.* **2011**, *133*, 9616−9625.

(17) Santner, S.; Wolff, A.; Ruck, M.; Dehnen, S. Multi-Valent Group 14 Chalcogenide Architectures from Ionic Liquids: 0D-$\{[Cs@Sn^{II}_4(Ge^{IV}_4Se_{10})_4]^{7-}\}$ and 2D-$\{[Sn^{II}(Ge^{IV}_4Se_{10})]^{2-}\}$. *Chem.—Eur. J.* **2018**, *24*, 11899−11903.

(18) Li, H.; Laine, A.; O'Keeffe, M.; Yaghi, O. M. Supertetrahedral Sulfide Crystals with Giant Cavities and Channels. *Science* **1999**, *283*, 1145−1147.

(19) Li, H.; Kim, J.; Groy, T. L.; O'Keeffe, M.; Yaghi, O. M. 20 Å $Cd_4In_{16}S_{35}^{14-}$ Supertetrahedral T4 Clusters as Building Units in Decorated Cristobalite Frameworks. *J. Am. Chem. Soc.* **2001**, *123*, 4867−4868.

(20) Zheng, N.; Bu, X.; Wang, B.; Feng, P. Microporous and Photoluminescent Chalcogenide Zeolite Analogs. *Science* **2002**, *298*, 2366−2369.

(21) Li, W.-A.; Peng, Y.-C.; Ma, W.; Huang, X.-Y.; Feng, M.-L. Rapid and Selective Removal of Cs^+ and Sr^{2+} Ions by Two Zeolite-Type Sulfides via Ion Exchange Method. *Chem. Eng. J.* **2022**, *442*, No. 136377.

(22) Yang, H.; Luo, M.; Luo, L.; Wang, H.; Hu, D.; Lin, J.; Wang, X.; Wang, Y.; Wang, S.; Bu, X.; Feng, P.; Wu, T. Highly Selective and Rapid Uptake of Radionuclide Cesium Based on Robust Zeolitic Chalcogenide via Stepwise Ion-Exchange Strategy. *Chem. Mater.* **2016**, *28*, 8774−8780.

(23) Yokoi, T.; Yoshioka, M.; Imai, H.; Tatsumi, T. Diversification of RTH-Type Zeolite and Its Catalytic Application. *Angew. Chem., Int. Ed.* **2009**, *48*, 9884−9887.

(24) Cooper, E. R.; Andrews, C. D.; Wheatley, P. S.; Webb, P. B.; Wormald, P.; Morris, R. E. Ionic Liquids and Eutectic Mixtures as Solvent and Template in Synthesis of Zeolite Analogues. *Nature* **2004**, *430*, 1012−1016.

(25) Freyhardt, C. C.; Tsapatsis, M.; Lobo, R. F.; Balkus, K. J.; Davis, M. E. A High-Silica Zeolite with a 14-Tetrahedral-Atom Pore Opening. *Nature* **1996**, *381*, 295−298.

(26) Wang, W.; Wang, X.; Hu, D.; Yang, H.; Xue, C.; Lin, Z.; Wu, T. An Unusual Metal Chalcogenide Zeolitic Framework Built from the Extended Spiro-5 Units with Supertetrahedral Clusters as Nodes. *Inorg. Chem.* **2018**, *57*, 921−925.

(27) Wu, Z.; Weigend, F.; Fenske, D.; Naumann, T.; Gottfried, J. M.; Dehnen, S. Ion-Selective Assembly of Supertetrahedral Selenido Germanate Clusters for Alkali Metal Ion Capture and Separation. *J. Am. Chem. Soc.* **2023**, *145*, 3802−3811.

(28) Lin, Y.; Massa, W.; Dehnen, S. Controlling the Assembly of Chalcogenide Anions in Ionic Liquids: From Binary Ge/Se through

Ternary Ge/Sn/Se to Binary Sn/Se Frameworks. *Chem.—Eur. J.* **2012**, *18*, 13427−13434.

(29) Mathieson, A.; Feldmann, S.; De Volder, M. Solid-State Lithium-Ion Batteries as a Method for Doping Halide Perovskites with an In Situ Optical Readout of Dopant Concentration. *JACS Au* **2022**, *2*, 1313−1317.

(30) Jin, M.; Zeng, Z.; Fu, H.; Wang, S.; Yin, Z.; Zhai, X.; Zhang, Q.; Du, Y. Strain-Negligible Eu^{2+} Doping Enabled Color-Tunable Harsh Condition-Resistant Perovskite Nanocrystals for Superior Light-Emitting Diodes. *JACS Au* **2023**, *3*, 216−226.

(31) Wang, X.-L.; Wu, Z.; Wang, X.; Xue, C.; Liu, C.; Zhang, J.; Zhou, R.; Li, D.-S.; Wu, T. Bifunctional Electrocatalysts Derived from Cluster-Based Ternary Sulfides for Oxygen Electrode Reactions. *Electrochim. Acta* **2021**, *376*, No. 138048.

(32) Lin, Q.; Bu, X.; Mao, C.; Zhao, X.; Sasan, K.; Feng, P. Mimicking High-Silica Zeolites: Highly Stable Germanium- and Tin-Rich Zeolite-Type Chalcogenides. *J. Am. Chem. Soc.* **2015**, *137*, 6184−6187.

(33) Zheng, N.; Bu, X.; Feng, P. Two-Dimensional Organization of $[ZnGe_3S_9(H_2O)]^{4-}$ Supertetrahedral Clusters Templated by a Metal Complex. *Chem. Commun.* **2005**, *22*, 2805−2807.

(34) Wang, Z.; Liu, Y.; Zhang, J.; Wang, X.; Wu, Z.; Wu, J.; Chen, N.; Li, D.-S.; Wu, T. Unveiling the Impurity-Modulated Photoluminescence from Mn^{2+}-Containing Metal Chalcogenide Semiconductors via Fe^{2+} Doping. *J. Mater. Chem. C* **2021**, *9*, 13680−13686.

(35) Wu, Z.; Wang, X.-L.; Wang, X.; Xu, X.; Li, D.-S.; Wu, T. 0D/2D Heterostructure Constructed by Ultra-Small Chalcogenide-Cluster Aggregated Quaternary Sulfides and g-C_3N_4 for Enhanced Photocatalytic H2 Evolution. *Chem. Eng. J.* **2021**, *426*, No. 131216.

(36) Zhao, X.-W.; Qian, L.-W.; Su, H.-C.; Mo, C.-J.; Que, C.-J.; Zhu, Q.-Y.; Dai, J. Co-Assembled T4-$Cu_4In_{16}S_{35}$ and Cubic Cu12S8 Clusters: A Crystal Precursor for Near-Infrared Absorption Material. *Cryst. Growth Des.* **2015**, *15*, 5749−5753.

(37) Rinn, N.; Guggolz, L.; Hou, H. Y.; Dehnen, S. Systematic Access of Ternary Organotetrel-Copper Chalcogenide Clusters by $[PhTE_3]^{3-}$ Anions (T = Si, Sn; E = S, Se). *Chem.—Eur. J.* **2021**, *27*, 11167−11174.

(38) Zhang, J.; Wang, X.; Lv, J.; Li, D.-S.; Wu, T. A Multivalent Mixed-Metal Strategy for Single-Cu^+-Ion-Bridged Cluster-Based Chalcogenide Open Frameworks for Sensitive Nonenzymatic Detection of Glucose. *Chem. Commun.* **2019**, *55*, 6357−6360.

(39) Yang, H.; Wang, L.; Hu, D.; Lin, J.; Luo, L.; Wang, H.; Wu, T. A Novel Copper-Rich Open-Framework Chalcogenide Constructed from Octahedral Cu_4Se_6 and Icosahedral Cu_8Se_{13} Nanoclusters. *Chem. Commun.* **2016**, *52*, 4140−4143.

(40) Kaib, T.; Bron, P.; Haddadpour, S.; Mayrhofer, L.; Pastewka, L.; Järvi, T. T.; Moseler, M.; Roling, B.; Dehnen, S. Lithium Chalcogenidotetrelates: LiChT—Synthesis and Characterization of New Li^+ Ion Conducting Li/Sn/Se Compounds. *Chem. Mater.* **2013**, *25*, 2961−2969.

(41) Lin, Y.; Dehnen, S. $[BMIm]_4[Sn_9Se_{20}]$: Ionothermal Synthesis of a Selenidostannate with a 3D Open-Framework Structure. *Inorg. Chem.* **2011**, *50*, 7913−7915.

(42) Sheldrick, G. M. Crystal Structure Refinement with *SHELXL*. *Acta Crystallogr.* **2015**, *C71*, 3−8.

(43) Spek, A. L. Structure Validation in Chemical Crystallography. *Acta Crystallogr.* **2009**, *D65*, 148−155.

(44) van der Sluis, P.; Spek, A. L. BYPASS: An Effective Method for the Refinement of Crystal Structures Containing Disordered Solvent Regions. *Acta Crystallogr.* **1990**, *A46*, 194−201.

(45) Eulenstein, A. R.; Bogdanovski, D.; Reinhardt, H.; Miß, V.; Roling, B.; Hampp, N.; Dronskowski, R.; Dehnen, S. $K_2Ge_3As_3$: Fiberlike Crystals of a Narrow-Band-Gap Zintl Phase with a One-Dimensional Substructure $_\infty{}^1\{(Ge_3As_3)^{2-}\}$. *Chem. Mater.* **2019**, *31*, 8839−8849.

(46) Boldish, S. I.; White, W. B. *Optical Band Gaps of Selected Ternary Sulfide Minerals.* **1998**, *83*, 865−871.

(47) Escobedo-Morales, A.; Ruiz-López, I. I.; de Ruiz-Peralta, M. L.; Tepech-Carrillo, L.; Sánchez-Cantú, M.; Moreno-Orea, J. E. Automated Method for the Determination of the Band Gap Energy of Pure and Mixed Powder Samples Using Diffuse Reflectance Spectroscopy. *Heliyon* **2019**, *5*, No. e01505.

(48) Dehnen, S.; Schäfer, A.; Fenske, D.; Ahlrichs, R. New Sulfur- and Selenium-Bridged Copper Clusters; Ab Initio Calculations on $[Cu_{2n}Se_n(PH_3)_m]$ Clusters. *Angew. Chem., Int. Ed. Engl.* **1994**, *33*, 746−749.

(49) Wang, C.; Haushalter, R. C. Synthesis and Structural Characterization of Two New Zintl $[M_7As_3Q_{13}]^{4-}$ Anions (M = Cu, Ag; Q = Se, Te) Containing Distorted Cubane $[M_7Q]$ Clusters. *Inorg. Chim. Acta* **1999**, *288*, 1−6.

(50) Wang, C.; Haushalter, R. C. A Discrete Cubane-like $[Cu_7Te]$ Cluster: Synthesis and Structural Characterization of $(NBu_4)_4Cu_7As_3Te_{13}$. *Chem. Commun.* **1997**, *15*, 1457−1458.

(51) Yaghi, O. M. Reticular Chemistry—Construction, Properties, and Precision Reactions of Frameworks. *J. Am. Chem. Soc.* **2016**, *138*, 15507−15509.

(52) Kong, Y.; Ding, Y.; Liu, C.; Zhang, J.; Zhou, R.; Li, D.-S.; Chen, N.; Wang, X.; Wu, T. A Novel Copper-Rich Open-Framework Chalcogenide with Chiral Topology Constructed from Distinctive Bimetallic $[Cu_5SnSe_{10}]$ Clusters. *Dalt. Trans.* **2021**, *50*, 14985−14989.

(53) Spek, A. L. PLATON SQUEEZE: A Tool for the Calculation of the Disordered Solvent Contribution to the Calculated Structure Factors. *Acta Crystallogr.* **2015**, *C71*, 9−18.

(54) Liu, C. W.; Sarkar, B.; Huang, Y.-J.; Liao, P.-K.; Wang, J.-C.; Saillard, J.-Y.; Kahlal, S. Octanuclear Copper(I) Clusters Inscribed in a Se_{12} Icosahedron: Anion-Induced Modulation of the Core Size and Symmetry. *J. Am. Chem. Soc.* **2009**, *131*, 11222−11233.

(55) Li, W.-A.; Li, J.-R.; Zhang, B.; Sun, H.-Y.; Jin, J.-C.; Huang, X.-Y.; Feng, M.-L. Layered Thiostannates with Distinct Arrangements of Mixed Cations for the Selective Capture of Cs^+, Sr^{2+}, and Eu^{3+} Ions. *ACS Appl. Mater. Interfaces* **2021**, *13*, 10191−10201.

(56) Peters, B.; Möbs, M.; Michel, N.; Tambornino, F.; Dehnen, S. Ionic Liquid-Driven Formation of and Cation Exchange in Layered Sulfido Stannates − a CH_2 Group Makes the Difference. *ChemistryOpen* **2021**, *10*, 227−232.

(57) Du, C.-F.; Li, J.-R.; Feng, M.-L.; Zou, G.-D.; Shen, N.-N.; Huang, X.-Y. Varied Forms of Lamellar $[Sn_3Se_7]_n^{2n-}$ Anion: The Competitive and Synergistic Structure-Directing Effects of Metal−Amine Complex and Imidazolium Cations. *Dalt. Trans.* **2015**, *44*, 7364−7372.

(58) Xiong, W.-W.; Miao, J.; Ye, K.; Wang, Y.; Liu, B.; Zhang, Q. Threading Chalcogenide Layers with Polymer Chains. *Angew. Chem., Int. Ed.* **2015**, *54*, 546−550.

(59) Jiang, T.; Ozin, G. A.; Bedard, R. L. Nanoporous Tin(IV) Sulfides: Mode of Formation. *Adv. Mater.* **1994**, *6*, 860−865.

(60) Liu, H.-W.; Wang, K.-Y.; Ding, D.; Sun, M.; Cheng, L.; Wang, C. Deep Eutectic Solvothermal Synthesis of an Open Framework Copper Selenidogermanate with PH-Resistant Cs^+ Ion Exchange Properties. *Chem. Commun.* **2019**, *55*, 13884−13887.

(61) Luo, M.; Hu, D.; Yang, H.; Li, D.; Wu, T. PCU-Type Copper-Rich Open-Framework Chalcogenides: Pushing up the Length Limit of the Connection Mode and the First Mixed-Metal $[Cu_7GeSe_{13}]$ Cluster. *Inorg. Chem. Front.* **2017**, *4*, 387−392.

(62) Zhang, R.-C.; Yao, H.-G.; Ji, S.-H.; Liu, M.-C.; Ji, M.; An, Y.-L. $(H_2en)_2Cu_8Sn_3S_{12}$: A Trigonal CuS3-Based Open-Framework Sulfide with Interesting Ion-Exchange Properties. *Chem. Commun.* **2010**, *46*, 4550−4552.

(63) Ahmadi, M.; Pramana, S. S.; Batabyal, S. K.; Boothroyd, C.; Mhaisalkar, S. G.; Lam, Y. M. Synthesis of Cu2SnSe3 Nanocrystals for Solution Processable Photovoltaic Cells. *Inorg. Chem.* **2013**, *52*, 1722−1728.

(64) Shi, L.; Pei, C.; Xu, Y.; Li, Q. Template-Directed Synthesis of Ordered Single-Crystalline Nanowires Arrays of Cu_2ZnSnS_4 and $Cu_2ZnSnSe_4$. *J. Am. Chem. Soc.* **2011**, *133*, 10328−10331.

(65) Li, B.; Xie, Y.; Huang, J.; Qian, Y. Synthesis, Characterization, and Properties of Nanocrystalline Cu_2SnS_3. *J. Solid State Chem.* **2000**, *153*, 170−173.

(66) Cai, X.; Jing, H.; Wuliji, H.; Zhu, H. Valence Band Structure Degeneracy Enhanced Thermoelectric Performance in β-Cu_2Se. *J. Phys. Chem. C* **2023**, *127*, 5576−5583.

(67) Gonzalez, J. M.; Oleynik, I. I. Layer-Dependent Properties of SnS_2 and $SnSe_2$ Two-Dimensional Materials. *Phys. Rev. B* **2016**, *94*, No. 125443.